Design, analysis and beam-wave interaction studies of fixed frequency (95 GHz 100kW CW, TE$_{10,4}$ mode) gyrotron operated in the volumetric mode

4.1. **Introduction**

4.2. **Design Constraints and Mode Selection of Gyrotron**

4.3. **Design of RF Interaction Cavity**

4.4. **Beam Wave Interaction Study**

    4.4.1. Time dependent multimode analysis with misalignment effects

        4.4.1a. Multimode analysis with ideal beam conditions

    4.4.2. 3D Particle in Cell (PIC) simulation

    4.4.3. Effect of electron velocity spread

4.5. **Design and Analysis with the Nonlinear Taper**

4.6. **Thermo-Mechanical Studies**

4.7. **Conclusions**

4.1. Introduction

In Chapter 3, the gyrotron device design constraints, linear theory and nonlinear theory used for the design and analysis of the cylindrical tapered interaction cavity gyrotrons have been described and demonstrated. As well as, the RF simulation study using commercial 3D PIC code "CST studio suite" and thermal studies using commercial PIC code "COMSOL Multiphysics" have been presented. It has been observed that, the thermal effects due to ohmic losses limits the margins of cavity dimensions tolerances and that necessitates the presence of cooling maintenance system for the high power devices. As well as, the shifts in the beam sources, i. e., misalignment of the beam axis with respect to cavity axis, are also found to limit the operation. Since, the dimensional and beam radius variations are also get scales with operating modes, so lower order mode gives small margin of tolerances, even though mode like, $TE_{6,2}$ is widely used at 95GHz frequency for 100 kW gyrotron, but observing these effects, we wants to investigate the advantages as well as challenges by operating this specification gyrotron device in the higher order volumetric modes, which is so far not fully explored and reported in the published literature, at least not accessible to us.

Considering the challenges and issues related to thermal and misalignments, in this chapter, Chapter 4, we designed, analyzed and simulated an RF interaction cavity for the same rating device that operates in a relatively high order mode $TE_{10,4\text{-}}$ that allows a wide transverse dimensions thereby more relaxation regarding thermal issues as well can be upgraded to high power levels too. In the literature, Krishna *et al.* (2011), have started the mode selection and the analysis of RF interaction cavity in the absence of electron beam but not much details about the beam wave interaction studies that includes RF analysis and thermal analysis as well the post interaction components, like, nonlinear taper, and RF window designs were not reported. Considering this gap,

additionally the goals mentioned in the Chapter 3, in the present work, the design, analysis and simulated the interaction cavity that gives the desired power in the operating mode $TE_{10,4-}$ and larger dimension relaxes the thermal issues is presented. After the design of interaction cavity by adding the nonlinear taper section, the beam wave interaction studies are revisited using time dependent multimode theory with uniform profile of magnetic field. The detailed design methodology, beam wave interaction studies are described in this chapter.

With the help of the theories presented in Chapter 3, the design constraints values for the various modes of the design beam parameters, the mode selection and the identification of the compete modes are determined as per the beam parameters Later on, using Vlasov approximation the RF cavity dimension was got determined.

In addition, the nonlinear taper that acts as impedance matching unit between interaction structure and the collector circuits and allows the transmission of generated RF power to the RF window with minimum mode conversion, is presented. In the present design, the NLT is designed such that quasi-optical mode converters can be used for transmitting interaction cavity mode TE_{mn} into free space Gaussian beam mode TEM_{00}.

Like the beam wave interaction studies in the interaction cavity region presented in Chapter 3, for the current design, by adding the nonlinear taper region, the beam wave interaction studies are performed. As well, the beam misalignment effects are incorporated into the time dependent multimode theory, the structures are analyzed. The NLT is confirmed through Vlasov approximation as well beam wave interaction studies allowing a constant uniform magnetic field profile. For the same, the 3D PIC

simulations, both for RF interaction as well as thermo-mechanical analysis are also performed integratedly here using a single tool "CST Studio Suite".

The Chapter has been organized as follows. Starts with the calculations of design constraints and the RF cavity dimensions using linear theories presented in Chapter 3, the beam wave interaction studies are performed using both analysis and 3D PIC simulation. The misalignment effects are added in the time dependent theory and the analysis is carried out for various beam widths. Followed by the design and analysis of the nonlinear taper (NLT) section and the beam wave interaction studies including NLT are presented. For the optimized cavity and NLT section, and the thermo-mechanical studies are reported.

4.2 Design Constraints and Mode Selection of Gyrotron

In Table 4.1, the design goals and constraints for the 95GHz, 100kW is outlined. Starting with the calculation of design constraints mentioned in Chapter 3, the suitable operating mode selection is carried out.

Table 4.1: Design goal and technical constraint values

Parameter	Value
Frequency f	95±0.1 GHz
Output power P_{out}	> 100 kW
Diffractive quality factor Q_{diff}	~2000
Beam current I_b	5 A
Beam voltage V_b	58 kV
Magnetic field at the cavity B	3.65±0.3 T
Pitch factor α	1.3-1.5
Harmonic number, s	1
Interaction efficiency η	>35%
Wall losses dP_{loss}/dA	< 2 kw/cm^2

Considering such design constraints and requirements of the device, a suitable operating mode selection is required for the achievement of the targeted goals. Sometimes, it is not feasible for modes to maintain all the design constraint within the limits and trade-off among constraints needs to be considered

In the present design, we are intending for the larger transverse dimension that relaxes the mode converter design as well further reduces ohmic losses that relaxes the need of the thermal management system thereby assurance of reliable device operation over longer period.

Table 4.2: Design constraints values for different modes

m	n	R_c (mm)	R_b (mm)	V_d (kV)	I_L (A)	Peak ohmic loss dP/dA (kW/cm^2)	m/X_{mp}	Δf_1	Δf_2
0	1	1.9256	0.9252	0.8198	49.841	6.188	0	51.9	109.1
2	1	1.5348	0.9252	0.5662	72.17	17.056	0.654	39.719	74.56
4	2	4.6649	2.1113	0.8868	46.08	1.295	0.430	13.651	8.039
5	2	5.2868	2.6723	0.7631	53.54	1.060	0.475	11.763	5.23
6	2	5.8975	3.2242	0.6754	60.49	0.893	0.511	10.354	3.31
6	3	7.6731	3.2242	0.9698	42.13	0.460	0.393	8.390	4.47
7	2	6.4993	3.7698	0.6092	67.07	0.768	0.541	9.259	1.93
7	3	8.3070	3.7698	0.8837	46.23	0.405	0.423	7.630	3.42
8	2	7.0939	4.3109	0.5571	73.34	0.671	0.566	8.382	0.910
8	3	8.9325	4.3109	0.8149	50.14	0.360	0.450	7.002	2.595
8	4	10.6689	4.3109	1.0136	40.31	0.234	0.376	6.063	3.07
9	2	7.6825	4.8484	0.5148	79.36	0.595	0.588	7.661	0.122
9	3	9.5510	4.8484	0.7584	53.88	0.324	0.473	6.475	1.932
9	4	11.3083	4.8484	0.9473	43.13	0.213	0.400	5.654	2.532
10	2	8.2661	5.3832	0.4797	85.17	0.532	0.608	7.059	0.494
10	3	10.1633	5.3832	0.7108	57.48	0.294	0.494	6.025	1.391
10	**4**	**11.9412**	**5.3832**	**0.8912**	**45.85**	**0.195**	**0.420**	**5.30**	**2.074**
10	5	13.6607	5.3832	1.0417	39.22	0.142	0.367	4.748	2.344
10	6	15.3455	5.3832	1.1718	34.87	0.109	0.327	4.309	2.436

A systematic procedure for suitable mode selection is adapted by considering a group of modes where azimuthal and radial indexes modes of up to 10. Considering effective length of the interaction cavity as 30.00 mm, at the design parameters listed in the above Table 4.1, using expressions (3.1) - (3.5) from Chapter 3, the design constraints for various modes are calculated and tabulated in Table 4.2.

Observing design constraints values for different modes, $TE_{0,1}$, and $TE_{2,1}$ modes can be eliminated owing to their smaller dimensions whose diameters are in the order of operating wavelengths, excessive Ohmic losses, respectively. There are several lower and higher order modes that can be suitable as an operating mode for the present design. But as stated above, in order to investigate the advantages of the larger transverse dimension of the RF interaction cavity structure on the RF performance, the asymmetric volume modes are suitable as the operating modes for the present problem. Considering low ohmic losses, larger transverse dimension and possibility of the implementation of the internal mode converters for the radial RF output coupling, $TE_{10,4-}$ mode is chosen as operating mode for the present study/design, where '-' and '+' indicates co-rotating and counter-rotating modes.

The limiting current I_L and voltage depression V_{dep} curves for the $TE_{10,4-}$ mode over a range of normalized beam radius values are calculated for the beam parameter listed in Table 4.1 and is plotted as Figure 4.1.
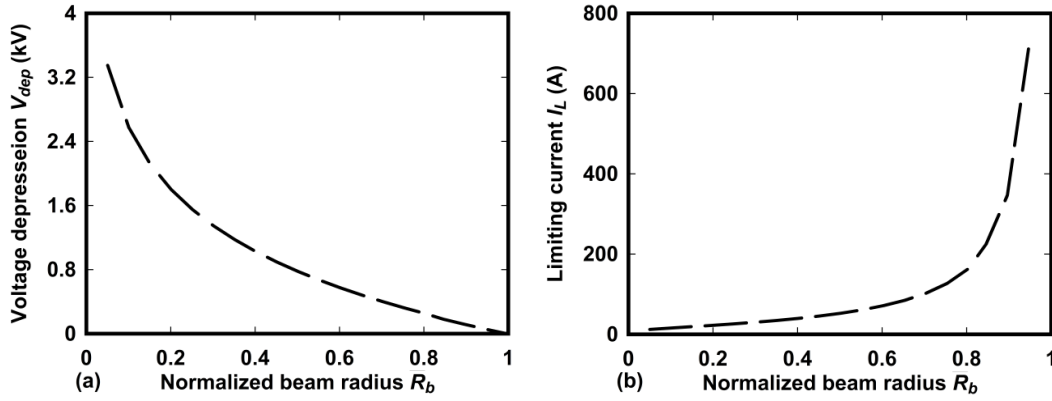
Figure 4.1: (a) Voltage depression V_{dep} (kV) versus normalized beam radius $\overline{R_b}(= R_b / R_c)$, and (b) Limiting current I_L (A) versus normalized beam radius $\overline{R_b}(= R_b / R_c)$ for $TE_{10,4-}$ mode.

After the selection of operating mode, the RF interaction cavity that provides space for the beam wave interaction has to be designed. The role of the interaction structure is to allow the growth of the operating mode at desired frequency of oscillation while suppressing the mode conversion when subjected to the beam parameters. The background analysis required for the RF cavity design and the selection of the cavity dimensions are presented in the following subsection.

4.3. Design of RF Interaction Cavity

As considered in Chapter 3.2, in the present design also, a conventional tapered cylindrical structure as RF interaction cavity is taken .The design of interaction cavity requires knowledge of axial RF field profile $V_{mp}(z)$, resonating frequencies f_{res}, and its quality factor Q_{diff}. By solving the Vlasov approximation equation using Numerov's methods, the interaction cavity geometries have been determined for several combinations.

Table 4.3: RF cavity parameter for various cavity combinations

Parameter	Set#1	Set#2	Set#3
L_d (mm)	15	15	15
L_c (mm)	28	30	32
L_{up} (mm)	10/15/20	10/15/20	10/15/20
θ_d	2^0	2^0	2^0
θ_{up}	1.8^0	1.8^0	1.8^0
L_{ds} (mm)	4	4	4
L_{us} (mm)	4	4	4
f_{res} (GHz)	95.035	95.01	94.985
Q_{diff}	1580	2250	2620
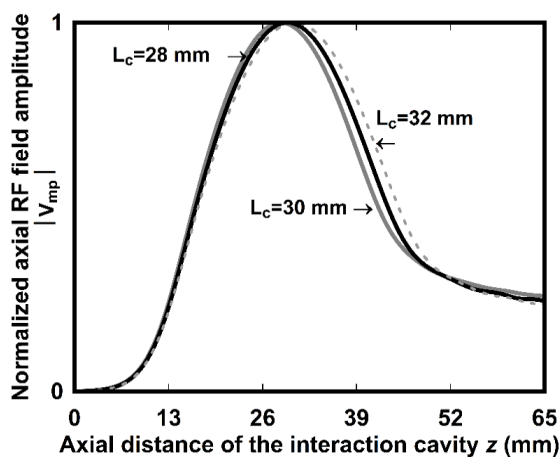
Figure 4.2: Normalized axial RF field amplitude profiles for various uniform section lengths: L_c= 28.00 mm (solid light), 30.00 mm (solid) and 32.00 mm (dashed light)

As described in Chapter 3, using a systematic cavity design procedure [Kalaria *et al.* (2016)], calculations is performed for various cavity geometry combinations. The suitable combinations and the corresponding cavity parameters in the cold condition (beam absent) i.e., J_{mp}= 0 are tabulated in Table 4.3.

The normalized axial RF field amplitude profiles for various uniform section lengths (L_c) are plotted in Figure 4.2. Longer cavity length provides longer interaction region, requiring lower beam current, however it results in larger quality factor Q_{diff}. Considering the advantages of lower beam current of operation and longer interaction

space over larger Q_{diff} values, the optimized interaction cavity dimensions are listed in Table 4.4.

Table 4.4: Optimized tapered RF cavity dimensions

Parameter	Value
Cavity radius R_c	11.94 mm
Down taper length L_d	15 mm
Middle section Length L_c	30 mm
Up taper length L_u	20 mm
Parabolic smoothing L_{ds}	4 mm
Parabolic Smoothing L_{us}	4 mm
Down taper angle θ_d	2^0
Up Taper angle θ_{up}	1.8^0
Resonant Frequency f_{res}	95.01 GHz
Diffractive quality factor Q_{diff}	2250

Following the determination procedure of probable RF cavity dimension, the designed beam parameter needs to be optimized such that accomplishment of desired operation with the minimum mode competition is achieved. Using the coupling coefficient and the start oscillations curves, the optimum beam radius and the possible compete modes are suitably identified. The values are calculated using the expressions (3.8) – (3.10), from Chapter 3 and the corresponding values are mentioned below.

The optimum beam radius is taken, such that, achieving maximum coupling and have significant distance away from both the walls as well axis of the structure. Considering various modes, the Coupling coefficient C_{mp} curves for various modes with respect to normalized beam radius $\overline{R_b} = R_b / R_c$ are shown in Figure 4.3. It can be observed that the maximum coupling for the desired mode TE$_{10,4}$- occurs at normalized beam radius $\overline{R_b}$ = 0.451, accordingly electron beam radius is selected as 5.38 mm.
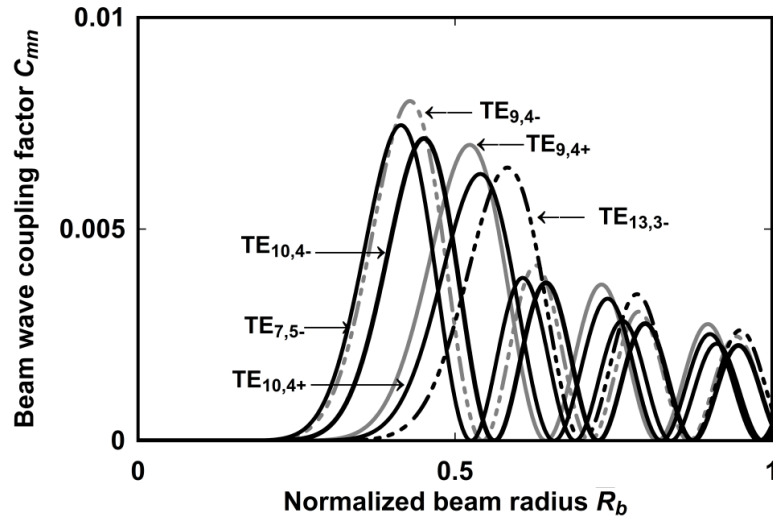
Figure 4.3: Beam wave coupling factor C_{mp} curves versus normalized beam radius ($\overline{R_b}$) for various modes.

Considering the beam parameter as mentioned in Table 4.1, the start oscillations curves for various modes for a range of magnetic fields from expressions (3.4) to (3.10) are calculated and are plotted in Figure 4.4.
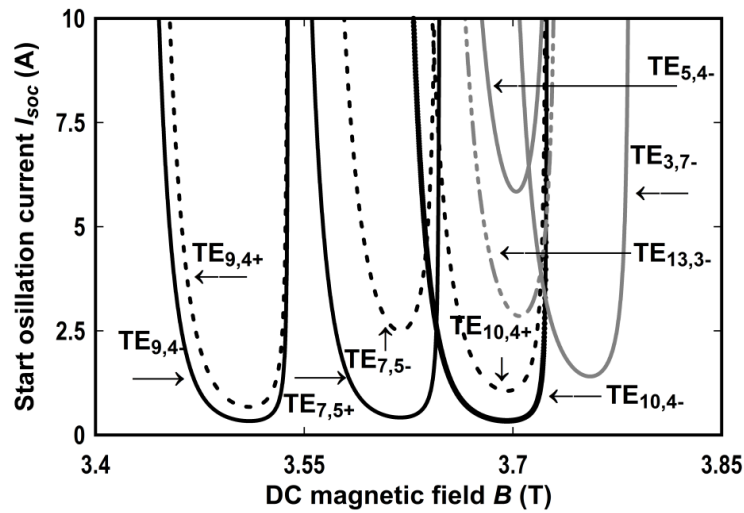

Figure 4.4: Start oscillation current I_{soc} (in amperes) versus DC magnetic field B in (Tesla) plots for different operating modes.

From the start oscillation current I_{soc} curves, it can be observed that $TE_{7,5+}$ is one of the main competing mode for the $TE_{10,4-}$, however a suitable selection of DC magnetic field can reduce its significance and are further examined during electron-beam and RF-wave interaction studies.

After determining the probable interaction cavity dimensions, the next step is to perform the beam wave interaction analysis that confirms whether the cavity is suitable and able to generate the desired power with suitable frequency. In the following section, using the time dependent multimode analysis mentioned in Chapter 3, the beam wave interaction analysis has been carried out and are explained in detail in the following section.

4.4. Beam-Wave Interaction Study

Taking the probable set of beam parameter and cavity dimension as obtained from Section 4.2, by studying the electron beam and RF wave interaction mechanism for operating mode along with competing modes, the design is to be confirmed with the optimized parameters. In the present section the beam wave interaction mechanism has been studied analytically using time dependent multimode analysis as well as through PIC simulation by CST studio suite.

4.4.1. Time-dependent multimode analysis with misalignment effects

In Chapter 3, the self-consistent time-dependent multimode nonlinear analysis developed by Fliflet *et al.* (1991) used for the study of the electron-beam and RF-wave interaction mechanism in the gyro devices is presented in detailed. In the theory the whole analysis has been carried out by considering axial symmetric gyrotrons i.e. both the beam and interaction cavity axis are sharing the same axis of symmetry as well are concentric to each other i.e., same centers. Practically, there might be situation where the concentricity does not meet, means beam axis either shifts or tilts with respect to the cavity frame. Hence, the beam wave interaction has to be studied considering these factors too for an efficient design. As in Chapter 3, these effects are investigated by 3D

144

PIC simulation but analytically using time dependent multimode theory has not been investigated.

The linear theory of the gyrotron with marginal shift of the beam axis with respect to cavity axis was developed and then generalized to coaxial cavities by Nusinovich *et al.* (2004), and Dumbrajs *et al.* (1995). Later, considering the beam tilt case, the theory was updated by Dumbrajs *et al.* (2013), and has discussed the effects with the help of self-consistent theory. With the help of this, we have updated/incorporated the addition factor that resulted due to the beam misalignments in the nonlinear, time dependent multimode theory developed by Fliflet *et al.* (1991), and the beam wave interaction studies are carried out. Secondly, the theory presented in Chapter 3 for multimode behaviour study in the interaction cavity, in the present chapter, by extending it to Nonlinear taper section, the after cavity interactions are by incorporating the original *h(z)* profile function derived by solving the Vlasov approximation equation.

The RF generations in the high power microwave sources, are strongly influenced by the coupling between electron beam and the rotating TE_{mpq} waves. For the strong synchronization, both the electron beam optical system axis and the microwave circuit axis, i. e., interaction cavity axis are in concentric to each other and any misalignments severely effects on the RF performance. In the present section, the role of misalignments on the beam wave coupling are studies and later these factors are incorporated in the time dependent multimode theory presented in the Chapter 3.

In axially symmetric gyrotrons, the coupling of electrons gyrating about a guiding center with a radial coordinate R_b to rotating TE_{mp} waves can be determined by the L_s and given by

$$L_s = J_{m-s}(k_t R_b) e^{-i(m-s)\psi} \qquad . \qquad (4.1)$$

Here, R_b is the radial coordinate of the guiding center in the cavity frame and ψ is the guiding angles of the beam. As describe in the Figure 3.7, the coordinates of the electron guiding centres in the cavity frame (R_b, ψ) and in the beam frame (R_0, ψ_0) in case of electron beam axis displacement of d with respect to cavity radius and are related as
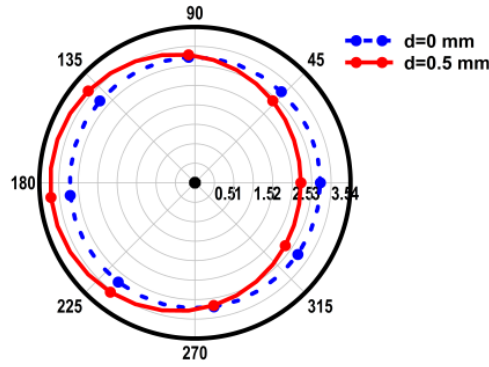
Figure 4.5: Beam misalignments effects: Location of beam lets for $d = 0$ *mm* and $d = 0.5$ *mm*.

$$R_0^2 = R_b^2 - 2dR_b \cos\psi + d^2 . \qquad (4.2)$$

The coupling of the beam with TE$_{m,p}$ wave in the case of displaced beam is given by:

$$L_S = \sum_{m_a=-\infty}^{\infty} J_{m_a}(k_\perp d) J_{m-s-m_a}(k_\perp R_b) e^{-i(m-s-m_a)\psi} \qquad . \qquad (4.3)$$

In the case of the parallel shift of the beam axis, the value of d is constant and independent of axial coordinate z. As well, assuming that the distance between two axes is always smaller than a wavelength, we can take account in the equation 4.3 only a limited number of terms, i. e., m_a value limits to few integer. In case of tilt in the beam axis, d varies with axial coordinate z and is given by :

$$d = \sqrt{(x_{00} + z\tan\alpha_x)^2 + (y_{00} + z\tan\alpha_y)^2} \qquad , \qquad (4.4)$$

where x_{00} and y_{00} are the transverse coordinates of the beam frame origin with respect to the origin of the resonator frame at the entrance and the angles $\alpha_{x,y}$ are the tilt angles in corresponding directions. Since x and y axes can be chosen arbitrarily, we can assume without a loss of generality that the beam is tilted in any one direction.

Hence, to describe the beam wave interaction in gyrotrons with a tilted beam by equations similar to those for a symmetric gyrotron, it is sufficient to introduce just one new function, which is the ratio of the beam coupling in a gyrotron with misaligned beam to that in a gyrotron with a concentric beam in the resonator mid-plane [Dumbrajs *et al.* (2013)]

$$T(z,\psi) = (\sum_{m_a} J_{m_a}\left[k_\perp(z)d(z)\right] J_{m-s-m_a}\left[k_\perp(z)R_0(z)\right] e^{im_a\psi}) / J_{m-s}(k_{\perp 0}R_{00}) \quad , \qquad (4.5)$$

and

$$k_t(z)R_0(z) = k_{\perp 0}R_0 \frac{R_c}{R(z)}\sqrt{\frac{B_{0,max}}{B_0(z)}} \qquad , \qquad (4.6)$$

where R_0 (z) is the beam radius in case of the misalignment and R_{00} is the beam radius under no misalignment.

By revisiting the Chapter 3 from, the electron trajectory equations (3.14) – (3.16) and the mode field phase and amplitude equations (3.17) – (3.19), the beam wave coupling factor f_n is updated with the new term resulted by equations (4.5) and (4.6).

Now, considering the misalignment effects, the normalized mode amplitude is updated by:

$$f_n = \frac{|e|}{m_e c^2} x_n' C_n J_{m_n-s}\left(k_{nt}r_b\right) a_n\left(t_0\right)\left|T(z,\psi)\right| \qquad (4.7)$$

and the phase terms in the equations $(3.14) - (3.16)$ gets an additional term $\angle T(z, \psi)$.

4.4.1a Multimode analysis with ideal beam conditions

As mentioned in Chapter 3, the coupled equations are numerically integrated using fourth order Runge-Kutta method. Considering a ramp type of DC beam voltage source from 35 kV to 58 kV with rise time duration of 150 ns is taken. DC beam voltage is applied to a uniformly distributed gyrating electron beam having 32 beamlets with 32 electrons in each beamlets. For the operating and its neighboring modes, like, $TE_{7,5}+$, $TE_{7,5}-$, $TE_{9,4}+$, $TE_{9,4}-$, $TE_{10,4}-$, and $TE_{10,4}+$ beam-wave interaction behaviour is observed and its temporal power growth P_m are determined (plotted as Figure 4.6). It can observed here that initially $TE_{7,5}+$ mode dominates and after 300 ns it dies out completely whereas the desired operating mode $TE_{10,4}-$ starts growing upto a stable RF power of ~123 kW; while all the competing modes reaches to a minimal value after 320 ns. An electronic efficiency of 40% is achieved at DC magnetic field of 3.65 T. Further, a parametric study is also performed analytically for range of applied DC magnetic fields and is discussed at the end of the section.
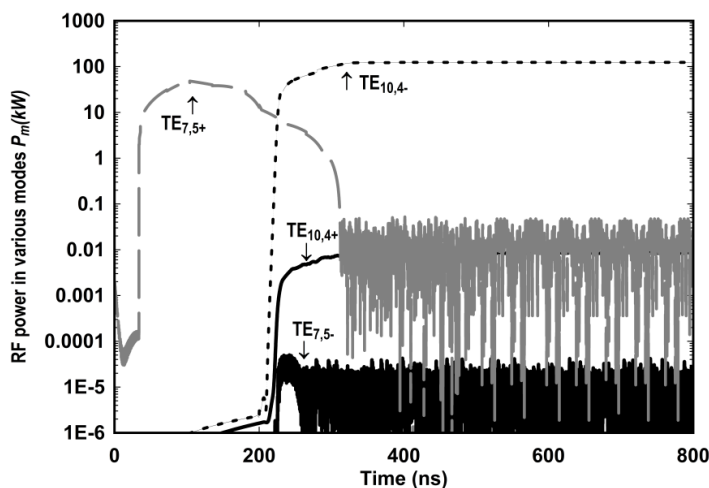

Figure 4.6: Temporal growth of output RF powers P_m (kW) in various modes through time dependent multimode analysis.

### 4.4.2. 3D Particle in cell (PIC) simulation

In addition, 3D Particle in Cell (PIC) simulation of the electron-beam and RF-wave interaction region of the device is performed reconfiguring a commercial code "CST Studio Suite". In the present study, taking OFHC copper as the cavity material with conductivity of 5.8×10^7 S/m, the RF interaction structure of the device is modeled. The lower conductivities yields more ohmic losses thereby challenges in the thermal system design which are discussed in detail in the thermal analysis section at the end of this Chapter. Like Chapter 3, A particle circular source is taken for forming the gyrating electron beam with designed beam parameters, and an external axial magnetic field profile *B(z)* is applied. To observe the temporal behaviour of modes, various 2D and 3D field monitors are placed with suitable boundary conditions.
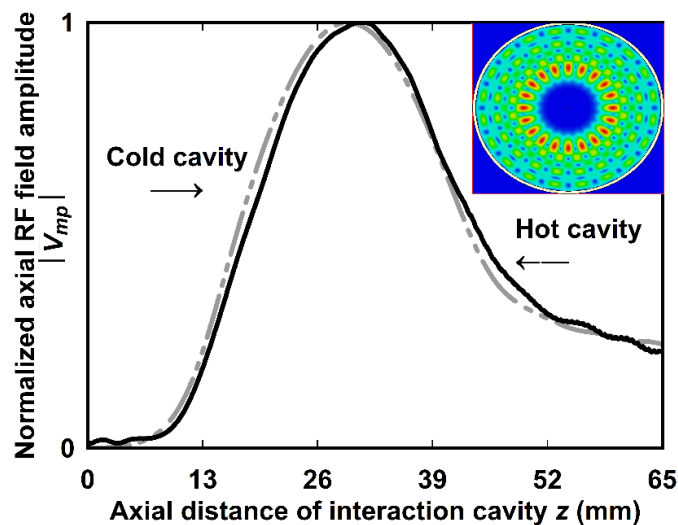
Figure 4.7: PIC simulation results: Comparisons of Normalized axial RF field amplitude profiles in the cold and hot conditions along with vector field distribution.

After the RF interaction cavity design, the desired axial electric field profile and mode excitation inside the cavity in the cold condition (absence of the electron beam) is ensured. Thereafter, by introducing the electron beam, the beam wave interaction

behaviour is investigated. The simulated interaction cavity axial RF electric field profile versus axial cavity position, for the cold (beam absent) and the hot (beam present) conditions, as vector plot is shown in Figure 4.7. It can be observed that here the field profile gets slight upward shift due to the beam loading. The time varying field amplitudes of various modes is also observed using 3D *E*-field monitors. Out of all the modes, the only significant amplitudes of the operating $TE_{10,4}$- mode and the main competing mode $TE_{7,5+}$, at magnetic field $B = 3.65$ T are plotted in Figure 4.8. Here, one can observe that for $TE_{10,4}$- operating mode RF signal growth stabilizes in 400 ns and competing $TE_{7,5+}$ mode decay to a minimal value in ~ 450 ns.
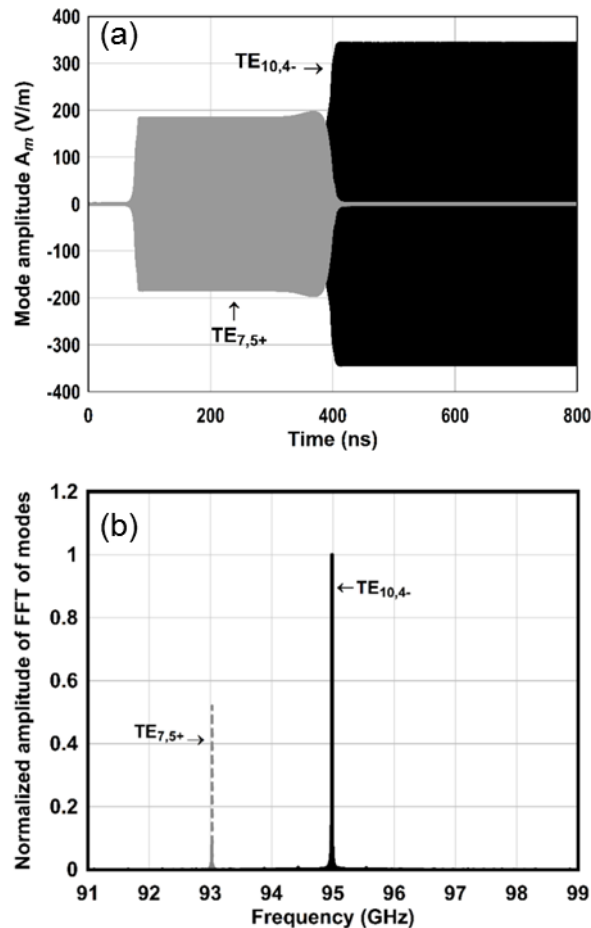
Figure 4.8: 3D PIC Simulation results- Temporal growth of operating and competing mode amplitudes A_m (V/m) from PIC Simulation study (b). Frequency response of the operating and compete modes.

In the next step, the post processing of the temporal power growth is performed for the $TE_{7,5+}$ and $TE_{10,4}$- modes and correspondingly their frequency responses are observed. The frequency response of the modes is determined by performing Fast Fourier Transform (FFT) action on the mode amplitude signals and the resultant response for the modes are shown in the Figure 4.8. It is observed that the FFT responses of the main mode $TE_{10,4-}$ and compete mode $TE_{7,5+}$ are significantly different both w.r.to to frequency as well amplitude levels. The oscillation frequency of the competing mode $TE_{7,5+}$ is significantly away from desired frequency of operation. A 2.0 GHz frequency separation from the main operating mode is observed and that confirms the mode competition is reduced through proper selection of the background DC magnetic field. As well from the peaks of the amplitudes of the FFT signals confirms that the $TE_{10,4}$- is dominant.

The temporal power growth in the gyrotron device for $TE_{7,5+}$ and $TE_{10,4}$- modes are shown in Figure 4.9, where one can readily observe that power transfer from the electron-beam to the RF-wave in different modes with time during device operation. Around 117 kW stable RF power is generated at oscillation frequency 94.98 GHz in at the desired operating $TE_{10,4}$- mode, while RF power generated in all the competing modes is less than a percent. A better view of the energy exchange from the electron beam to the RF wave can be observed from the wave particle power transfer with respect to time, as shown in Figure 4.10, which indicates the transfer of electron beam power to the RF wave in the time axis.
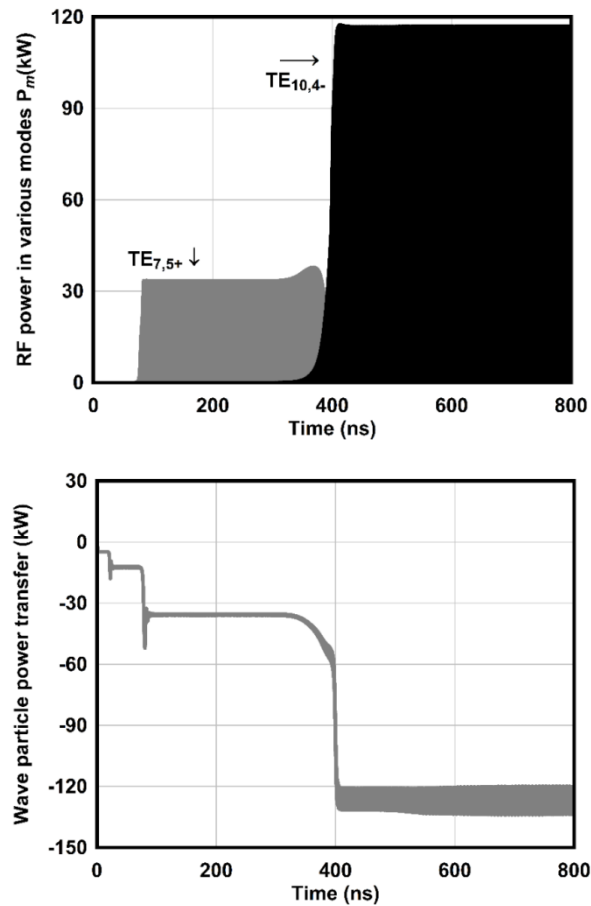
Figure 4.9: 3D PIC Simulation results-(a)Temporal growth of RF powers in the operating and competing modes P_m resulted from PIC simulation (b) Wave particle power transfer (kW) versus time (ns).

It can be further observed that from the start of simulation onwards, the electron beam loses its net power to the RF wave due to beam wave interaction continuously and reaches to a saturation level of more than >120 kW power to the RF wave after 400 ns. By correlating Figures 4.7 and 4.9, one can also observe that initially the beam losses its majority of the power/energy to the compete mode of the design, i. e., to $TE_{7,5+}$ time interval in between 100 ns to 300 ns until, the main mode $TE_{10,4+}$ is in the silent state. While in the transition period from 300 ns to 400 ns, the electron beam starts losing much more power to the RF wave growth simultaneously the mode $TE_{7,5+}$ also starts decaying where as the main mode starts growing and reaches to a stabilized value after 400ns. In order to show the stability as well less mode conversion of the

design, the beam wave interaction mechanisms through PIC simulation is carried out till 800 ns and found device saturated RF power as 117 kW.

### 4.4.3 Effect of the electrons velocity spread

The device performance is often required to be evaluated under non-ideal but in practical situations. Velocity spread in the electron beam is always present in the electron-beam devices and causes deviations in the beam characteristics and affects device performance. Even though, in present days, the device fabrication and beam launching technologies as well as facilities are considerably improved, which has reduced the amount of velocity spread but certain percentage of beam velocity spread is always present in the practical devices. In our study considering velocity spreads of 0%, 5% and 8%, its effect on the device performance is also evaluated. Using PIC simulation, the RF power and frequency of oscillations are calculated and tabulated in the Table 4.5. It is observed that the velocity spread effects much on the power level but its effect on oscillation frequency deviation is mild.

Table 4.5: RF power and frequencies for different velocity spreads

Velocity spread	RF power (kW)	Frequency (GHz)
0 %	117	94.98
5 %	112	94.968
8%	94.8	94.954

To strengthen the design study, a parametric analysis of device operation is also carried out for a range of the applied DC magnetic field. The RF output power generated versus applied DC magnetic field is performed both analytically and also compared for its validation with PIC simulated values (Figure 4.10). As magnetic field increases the RF power levels in the main mode are decreases in both analytical and

simulated results. Furthermore, an agreement within 7% is observed between the analytical and PIC simulation results.
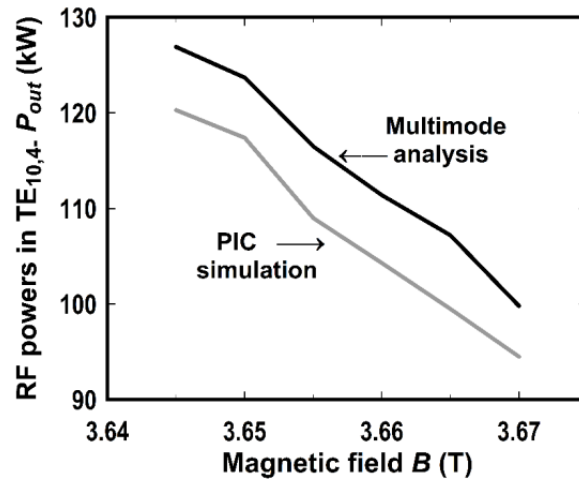
Figure 4.10: Comparisons of output RF powers in the main mode $TE_{10,4-}$ through multimode analysis and PIC simulation study.

By this, the RF cavity designed for the generation of 95 GHz, 100kW operating $TE_{10.4-}$ mode has been studied under ideal beam and velocity spread conditions.

In this chapter, the beam wave interaction studies for the proposed RF cavity with $TE_{10,4-}$, 95 GHz gyrotron are carried out for no misalignment and with misalignment by analytical approach as well PIC simulations with a uniform magnetic field profile along the interaction cavity.

With the help of the analysis mentioned in Section 4.4.1, the beam wave interaction studies in the presence of misalignment of beam axis with respect to cavity axis is performed by updating the time dependent multimode analysis as well as through simulations using 3D PIC commercial code.

The misalignment of beam axis from 0.00 mm to 0.50 mm with 0.25 mm are induced and the beam wave interactions behaviour got studied using analytical expressions and the observed figures in the main mode are calculated and tabulated in

Table 4.6. It's been observed that as the shift of the misalignment increases from 0.00 mm to 0.50 mm, the RF power in the desired mode reduces in a big way as well the efficiency too.

Table 4.6: RF power in the main with various beam misalignments

Beam shift d (mm)	RF power Analytical	RF power PIC code
0	123kW	109 kW
0.25	117 kW	115kW
0.5	106.5 kW	104 kW

4.5 Design and Analysis with the Nonlinear Taper

After the design and analysis of RF interaction structure, the generated RF power is carried to outside via nonlinear taper (NLT), quasi optical mode converter (radial output coupling) and RF window while the spent electron beam is collected by using a collector. Usually, for the preliminary design study of gyrotron oscillators, typical resonator geometry is being used that contains a down taper followed by a uniform mid-section and a linear uptaper. But to guarantee stable operation of the device, NLT should also be included in the calculations as an integral part of the resonator cavity and the NLT part should be designed carefully to minimize the mode conversion. Since, the QOMC converter follows the NLT section, and the launcher radius is usually related to mid-section radius by $1.07R_c$ to $1.1R_c$ times.

Coming to the design of nonlinear taper section used in gyrotrons, a raised cosine type of nonlinear section, with input radius a_1, end radius a_2 of length L_{NLT} and shape factor s_h are used in gyrotron oscillators and is given by

$$R(\mathbf{z}) = a_1 + \frac{(a_2 - a_1)}{2} \left\{ -1 + 2\left(\frac{z}{L_{NLT}}\right)^{s_h} + \frac{1}{\pi} \sin\left(\pi\left[-1 + 2\left(\frac{z}{L_{NLT}}\right)^{s_h}\right]\right) \right\} + \frac{(a_2 - a_1)}{2} \quad .$$

(4.8)

In the present work, by fixing the end radius of nonlinear taper as $R_{NLT} = 13.134$ mm, i. e., $1.1R_c$, and applying the Vlasov approximation theory presented in Chapter 3, on the combination of interaction cavity and the NLT, for various combinations of shape factors and NLT section lengths, the cold cavity field profiles and the corresponding cavity features i.e., resonant frequency and diffractive quality factors are calculated. Even, the uptaper lengths determined from the above section are varied so that achieving the energy conversion with optimum dimensions in less time.

By using the time dependent multimode theory reported in Chapter 3, for the RF cavity and NLT combinations, the beam wave interactions behaviour that is after cavity interactions are investigated analytically as well through 3D PIC simulation code. The calculations have been performed by allowing the radius profile as well complete cold cavity field profile $h(z)$ with uniform magnetic field profile $B(z)$.

By solving the Vlasov approximation equation, we determined few combinations of RF cavity and raised cosine type NLT profiles that can results the desired operation and are tabulated in Table.4.6.The time dependent multimode theory has been used for the after cavity interaction studies considering various compete modes. As well, it has been observed that the three cavities are resulting almost same diffractive quality factor and cold cavity resonating frequency combinations.
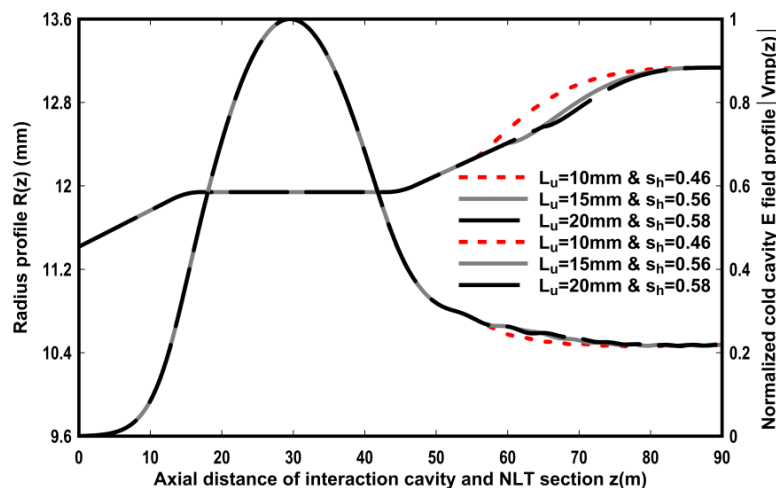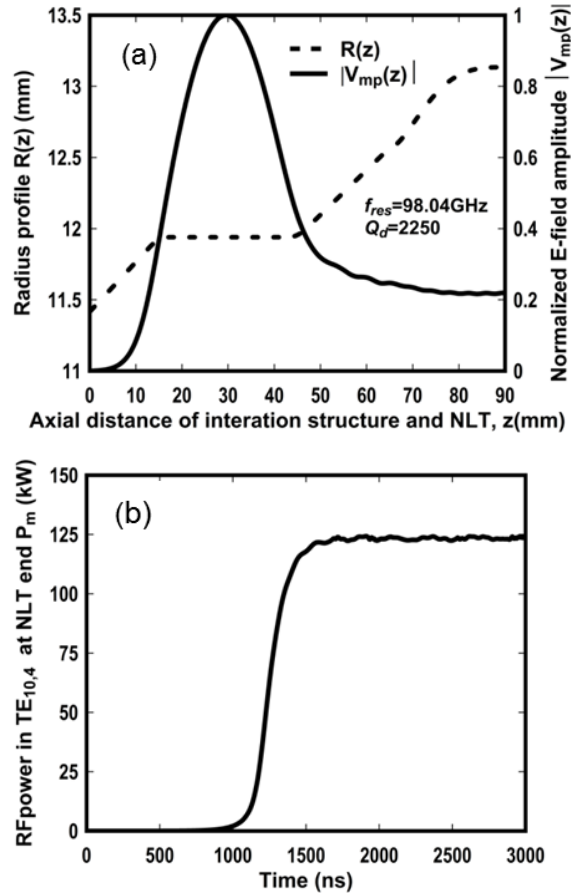
Figure 4.11: Normalized axial cold cavity field profiles and the corresponding radius profiles that include NLT section vs axial distance of the device.

**Table 4.7:** RF interaction cavity and NLT specifications

Parameter	Values		
R_C (mm)	11.94		
L_d (mm)	15		
L_c (mm)	30		
θ_d (^{o}) / θ_{up} (^{o})	2/1.8		
L_u (mm)	20	15	10
L_{NLT} (mm)	25	30	35
Shape factor, s_h	0.58	0.58	0.46
R_{NLT}(mm)	13.134		
Q_{diff} / f_{res} (GHz)	2250 /95.054		

The beam wave interaction analysis has been carried out for the above three profiles that looks suitable for the corresponding design. The RF power develop in the main mode along with the optimum radius profile based on the power growth and the less mode competition, the uptaper length has been chosen as 10 mm and are shown in Figure 4.12.

Figure 4.12: Analytical results: (a) normalized axial cold cavity field profiles and the corresponding radius profiles that include NLT section vs axial distance of the device (b) RF power versus time.

The 3D PIC simulation studies using Commercial CST Studio Suite after inclusion of NLT section to the RF interaction cavity with uniform magnetic profile are presented below. It has been observed that with uptaper of 10 mm and $L_{NLT} = 35.00$ mm, the beam wave interaction mechanism shows a quick growth in the desired mode as well a less time of compete mode presence in the simulation duration. The hot (electron beam present) cavity axial E field profile along with the vector field plot of the $TE_{10,4-}$ mode is shown in Figure 4.13.
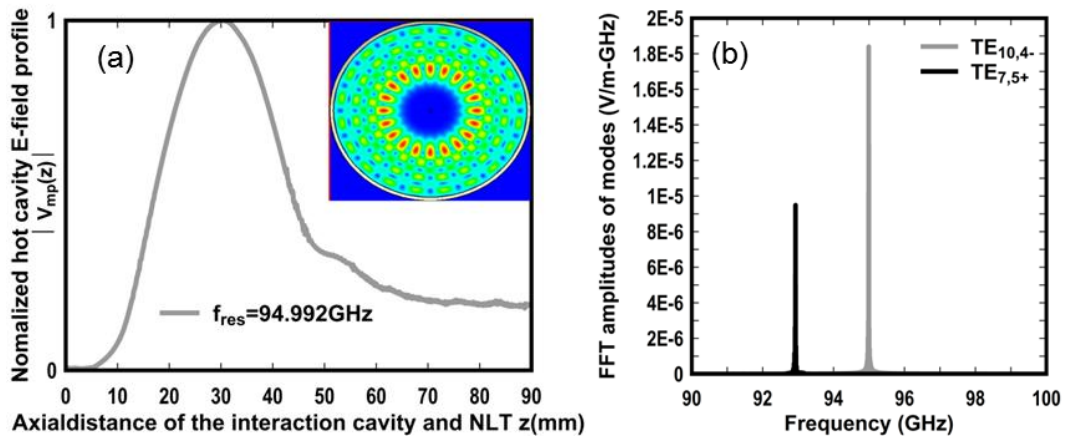
Figure 4.13: (a). Normalized axial E field profile in hot (beam present condition) along with 2D vector field pattern of $TE_{10,4-}$ mode (b). FFT field amplitudes of $TE_{10,4-}$ (Light shade) and $TE_{7,5+}$ (dark shade)modes.
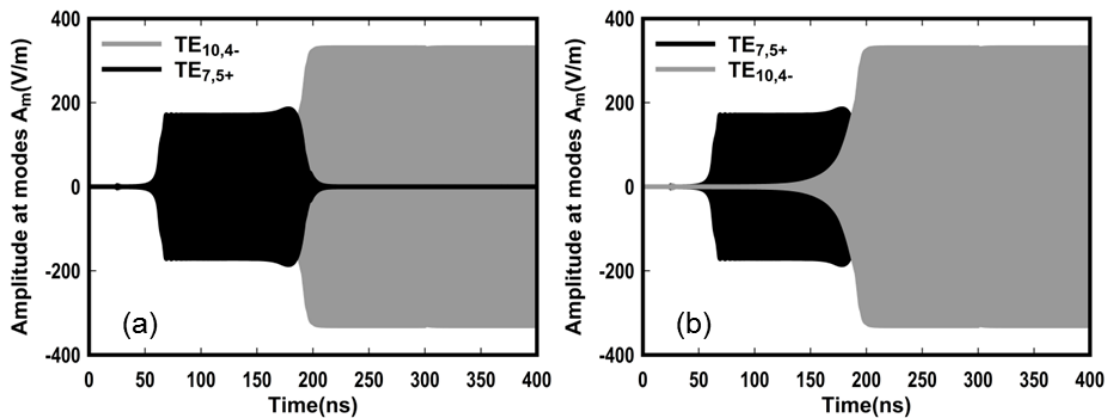
Figure 4.14: 3D PIC Simulation results- temporal growth of amplitudes across various modes A_m(V/m) (a) : $TE_{7,5+}$ overrides $TE_{10,4-}$ (while plotting) (b) vice versa.

It is observed that the desire mode oscillating with frequency of 94.99GHz as well the oscillating frequency of compete mode is far of more than 2GHz from operating frequency. The temporal growth of mode amplitudes and the corresponding RF power developed across various modes with respect to time has been calculated by post processing the results and are plotted in Figures 4.14 and 4.15.
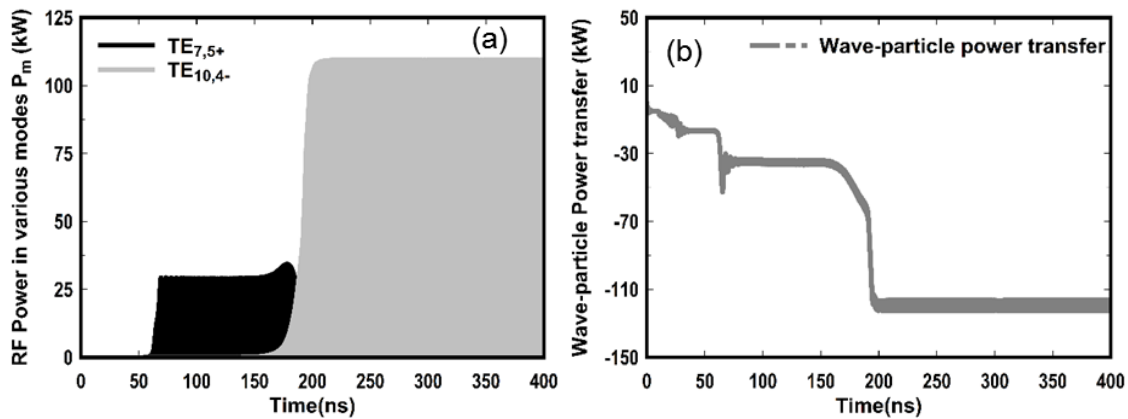
Figure 4.15: 3D PIC Simulation results- (a) temporal growth of mode powers and (b) wave particle power transfer versus time.

4.6. Thermo-Mechanical Analysis

As reported in Chapter 3 that thermo-mechanical analysis was simulated separately using commercial code "COMSOL Multiphysics". However, the thermo-mechanical analysis for the present case of the $TE_{10,4-}$ 100kW gyrotron including nonlinear taper section is performed using a single code "CST Studio Suite". With the experience of the Chapter 3, the analysis is carried out here also for two different electrical conductivities by considering two different electrical conductivities of the cavity material i.e., for 5.8e7 S/m and 2.9e7 S/m. The analysis is started by calculating the ohmic loss profile that acts as heat load of the structure by using the design parameters mentioned in Table 4.6, using equations (3.27). In the present design, the thermal effects are studied. Since, the value of the ohmic loss magnitude are varies as per the conductive nature of the cavity material, the present structure has been analysed for the both values. As per equation (3.27), the wall loading profiles along the interaction structure are plotted below Figure 4.16.
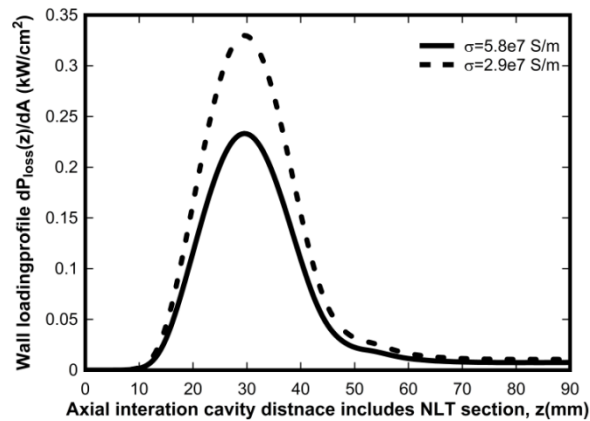
Figure 4.16: Ohmic loss profile for both the electrical conductivities for the cavity and NLT section.

Later on, by considering the cavity material with the properties as mention in Table 3.7, Chapter 3, the RF structure has been modelled. Initially, the structure has been subjected by various convective heat transfer coefficient h values and different cavity thickness dR values for determining the optimum combinations of h and dR values. Unlike in the Chapter 3, since for the measure of thermal effects the maximum inner radial deformations and outer surface temperatures are sufficient. Thereby, in the current analysis the effects are measured in terms of maximum values. Without much in detailed description like done in the Chapter 3, here, the thermal effects are calculated by modelling, suitable selection of boundary conditions.
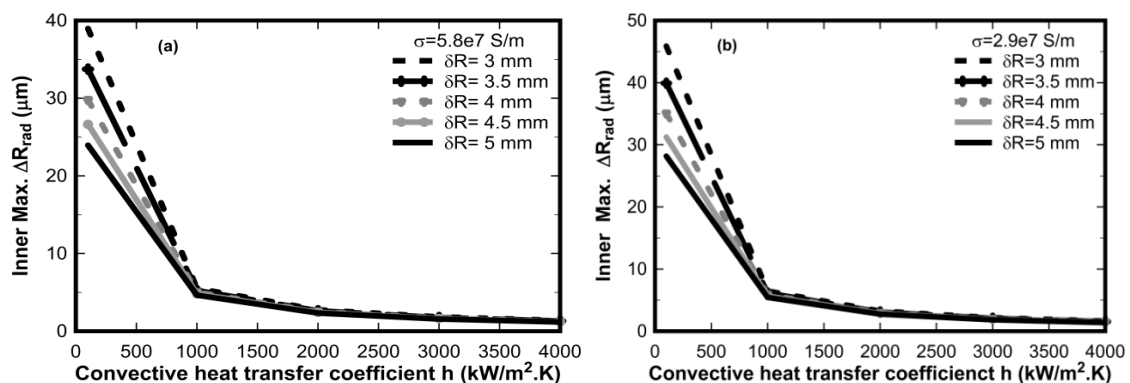

Figure 4.17: Inner maximum radial deformations versus convective heat transfer coefficient h for various cavity thickness δR_{rad} at electrical conductivities (a) 5.8e7 S/m (b) 2.9e7 S/m.
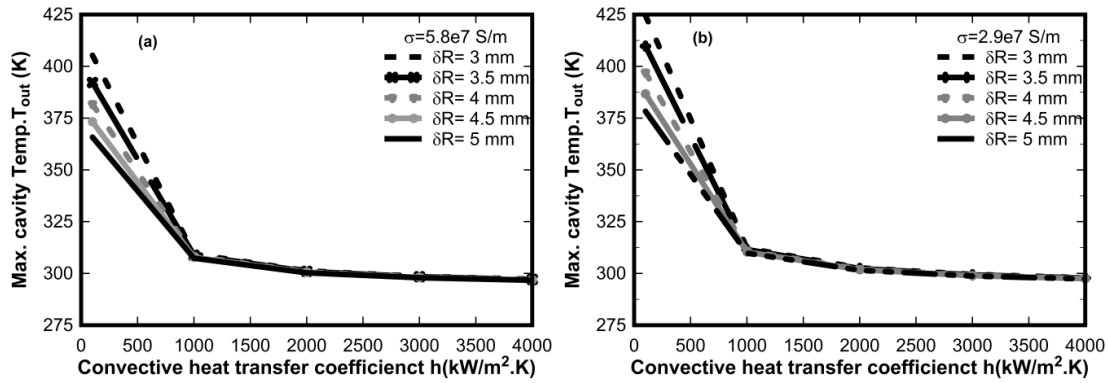
Figure 4.18: Outer maximum radial cavity temperatures T_{out} (K) versus convective heat transfer coefficient h at various cavity thickness δR_{rad} at electrical conductivities (a) 5.8e7 S/m (b) 2.9e7 S/m.

The Maximum deformations ΔR_{rad} at the inner surface and the temperatures T_{out} at the outer surfaces for various combinations of convective heat transfer coefficient *h* and cavity thickness δR values for the electrical conductivities $\sigma = 5.8e7$ S/m and 2.9e7 S/m are plotted in Figures 4.17 and 4.18. It can be observed from these figures that with $h \geq 1000$ and for any combination of δR value, the maximum radial deformation for both conductivities is near by 5 micrometres as well the maximum outer surface temperature is 310ºK whose values are quite promising as compared to $TE_{6,2}$ mode gyrotron, as discussed in Chapter 3. Since, in the present design, a max of 0.1 GHz frequency shift happens for the radial deformation of ~13 micrometres, keeping in mind about the nonlinear section module, the optimum cavity thickness is chosen as minimum of 4.5micrometers as well the optimum *h* is chosen around 2000 that results a maximum temperature of ~302 K and 2.5micrometers of inner deformations which are in tolerable limits.
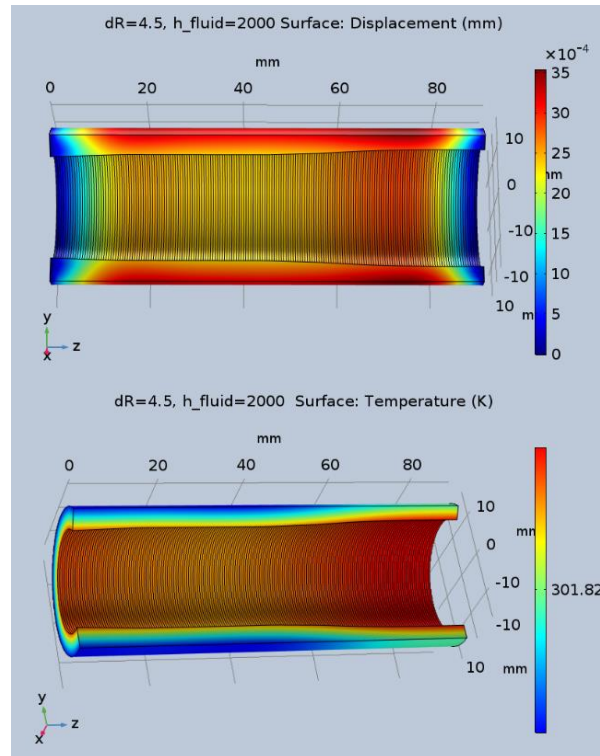
Figure 4.19: 3D view of surface displacements and surface temperatures for heat transfer coefficient h=2000 (W/m^2.K) and cavity δR= 4.5 mm.

Comparing with the TE$_{6,2}$- mode, 95 GHz gyrotron, the TE$_{10,4}$- mode operated gyrotron has less thermal effects on the system performance as well a very simple cooling system design requirements which even managed without any extended heat surfaces called Fins. With minimum/low values of thermal system parameters, the cooling system can be provide for reliable device performance which can reduce the complexity as well cost of the thermal system. Since, the thermal effects are very much under desire limits that's why its effects on the RF behaviour after optimized cooling system has not been discussed.

4.7. Conclusion

Keeping the goal of design and analysis of the gyrotron oscillator that able to generate 100kW at 95GHz that operates in the high order volumetric mode and does not require additional cooling system for its thermal management. The device is designed

for its operation at a higher order mode so as its RF interaction cavity structure dimension becomes larger and heat loading problem get relaxed. The operating mode selection has been carried out by inspecting the various design constraints. Later, using Vlasov approximation, the RF interaction cavity has been determined such that it able to provide desired sustainable growth of RF signals. Using time dependent multimode theory and simulations using PIC codes for the beam wave interaction studies has been carried out and able to observe that the desired performance at the end of the interaction cavity. To determine the optimum interaction cavity dimension as well the quasi optical mode launcher design, the cavity has been extended by adding a raised cosine type NLT section that acts as impedance matching unit between the RF cavity and the quasi optical mode converter and allows the RF transmission with minimum mode conversion.

The Vlasov approximation analysis of single mode has been used for the determination of the NLT profile. The same profile has been confirmed using after cavity beam wave interaction studies by extending the time dependent multimode theory of Fillet *et al* (1991), while taking the complete $h(z)$ profile calculated resulted from the Vlasov approximations analysis.

For the same radius profile, using PIC simulation, the after cavities interactions with uniform magnetic profile are carried out and results have been in good agreement with the analytical values. Later, the misalignment of beam axis with respect to cavity axis has also been analyzed by updating the time dependent theory with the modified beam wave coupling term and also simulated using PIC code. Then the thermal behaviour of the current design is studied and the optimum cooling parameters are determined now using an integrated tool, CST Studio suite. Further, it has also been observed that by operating the device in high order mode, the sensitivity of the device

for misalignments has been reduced. As well the impact of ohmic losses has been reduced significantly thereby requirement and challenges of cooling system.

With this complete design, analysis and simulations for beam wave interaction behaviour, it has been established that the designed 100kW, 95GHz gyrotron operating at the $TE_{10,4-}$ mode does not require external cooling system. In other side, the structure is needed to be investigated with the non-uniform magnetic profile. As well, efficiency of the device is found ~35%.